ACS NANO

www.acsnano.org

ARTICLE

Tuning the Lattice Parameter of In_xZn_yP for Highly Luminescent Lattice-Matched Core/Shell Quantum Dots

Francesca Pietra,*[,†] Luca De Trizio,[‡] Anne W. Hoekstra,[†] Nicolas Renaud,[†] Mirko Prato,[‡] Ferdinand C. Grozema,[†] Patrick J. Baesjou,[∥,⊥] Rolf Koole,[∥] Liberato Manna,[‡,§] and Arjan J. Houtepen[†]

[†]Optoelectronic Materials Section, Faculty of Applied Sciences, Delft University of Technology, Julianalaan 136, 2628 BL Delft, The Netherlands

[‡]Department of Nanochemistry, Istituto Italiano di Tecnologia (IIT), via Morego, 30, 16163 Genova, Italy

[§]Kavli Institute of Nanoscience, Delft University of Technology, Lorentzweg 1, 2628 CJ Delft, The Netherlands

[∥]Philips Research Laboratories, High Tech Campus 4, 5656 AE Eindhoven, The Netherlands

[⊥]Soft Condensed Matter, Debye Institute, Utrecht University, Princetonplein 5, 3584 CC Utrecht, The Netherlands

Supporting Information

ABSTRACT: **Colloidal quantum dots (QDs) show great promise as LED phosphors due to their tunable narrow-band emission and ability to produce high-quality white light. Currently, the most suitable QDs for lighting applications are based on cadmium, which presents a toxicity problem for consumer applications. The most promising cadmium-free candidate QDs are based on InP, but their quality lags much behind that of cadmium based QDs. This is not only because the synthesis of InP QDs is more challenging than that of Cd-based QDs, but also because the large lattice parameter of InP makes it difficult to grow an epitaxial, defect-free shell on top of such material. Here, we propose a viable approach to overcome this problem by alloying InP nanocrystals with Zn^{2+} ions, which enables the synthesis of In_xZn_yP alloy QDs having lattice constant that can be tuned from 5.93 Å (pure InP QDs) down to 5.39 Å by simply varying the concentration of the Zn precursor. This lattice engineering allows for subsequent strain-free, epitaxial growth of a $ZnSe_zS_{1-z}$ shell with lattice parameters matching that of the core. We demonstrate, for a wide range of core and shell compositions (*i.e.*, varying *x*, *y*, and *z*), that the photoluminescence quantum yield is maximal (up to 60%) when lattice mismatch is minimal.**

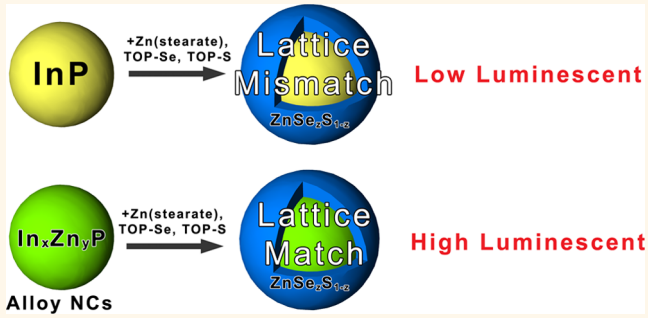

KEYWORDS: *quantum dots, core/shell heterostructures, In(Zn)P, lattice mismatch, alloy nanocrystals, phosphors*

Colloidal quantum dots (QDs) have attracted considerable interest for use in optoelectronic and biomedical devices, due to their unique optical and electrical properties.[1−3] In particular, QDs are seen as ideal candidates to replace current (red) phosphors in LEDs as they could significantly enhance the LED efficiency and color purity due to their tunable narrow-band emission.[3,4] For QDs to be employed in lighting applications they must have the stringent requirements of high photoluminescence (PL) quantum yield (QY) and high stability. While these requirements have been met, to a high degree, for Cd based QDs,[5,6] the toxicity of cadmium is a major issue for consumer applications. InP-based QDs are among the most investigated nontoxic Cd-free systems, owing to their comparable emission range.[7−26] However, in terms of PL QY and PL stability, they cannot yet compete with Cd-based QDs.

The predominant strategy for achieving higher PL efficiency is to grow a shell of a wider band gap material around the QD core, resulting in core/shell particles.[1] The shell material must be carefully chosen, not only in terms of band gap and relative positions of valence and conduction band edges with respect to those of the core, but also in terms of crystal structure and lattice parameter, in order to prevent the buildup of an excessive strain at the core−shell interface that would result in poor PL QY of the final QDs.[1,2,27,28] Therefore, finding

Received: February 19, 2016
Accepted: April 11, 2016
Published: April 11, 2016

DOI: 10.1021/acsnano.6b01266
ACS Nano 2016, 10, 4754−4762

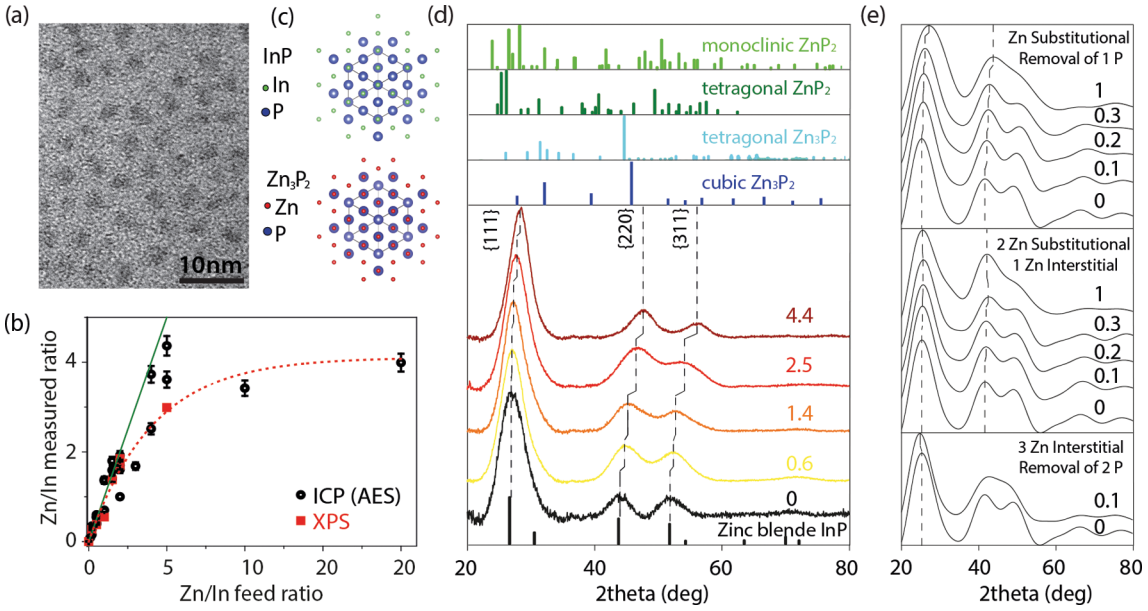

Figure 1. (a) TEM image of InP QDs. (b) Plot of the Zn/In ratio measured in InxZnyP QDs as a function of the corresponding precursors feed ratio. The plot follows a linear trend (green line) up to Zn/In = 5 after, after which the Zn/In ratio reachs saturation (red dashed line). The relative amounts of In and Zn were measured using ICP-OES elemental analysis (black empty dots) and confirmed by XPS (red solid squares). (c) Atomic scheme representing a (111) lattice facet of InP (upper panel) and Zn_3P_2 (lower panel) cubic phase. This shows that the P sublattice in Zn_3P_2 is the same as for InP. (d) XRD patterns obtained from drop-cast solutions of InxZnyP QDs, with different Zn/In ratios. The corresponding bulk reflections of zinc blende InP (black, ICSD code 24517), tetragonal Zn_2P (dark green, ICSD code 24487) and monoclinic Zn_2P (light green, ICSD code 60011), tetragonal Zn_3P_2 (light blue, ICSD code 250159), and cubic Zn_3P_2 (dark blue, ICSD code 24487) are reported in the lower and upper panels, respectively. (e) DFT-calculated XRD patterns of InxZnyP (1.5 nm) QDs considering Zn^{2+} as substitutional (upper panel), substitutional + interstitial (middle panel), or interstitial (lower panel) dopant in the zinc blend InP crystal structure.

strategies to avoid defect formation during the shell growth represents one of the main challenges in the field of nanomaterials for lighting applications. In this regard, InP presents an additional limitation: it has a large lattice constant (a = 5.93 Å), which makes it incompatible with standard shell materials (*i.e.*, GaP, a = 5.45 Å;[29] ZnS, a = 5.42 Å;[30] ZnSe, a = 5.66 Å[30]). In the past decades, strategies to overcome this problem have focused on adapting these shells to better match the InP core by the use of a graded core−shell interface, or the growth of an intermediate buffer layer to ensure low lattice strain.[13−16] However, these strategies necessitate additional steps in the fabrication of core/shell QDs, thereby increasing the complexity of the synthetic procedure. Additionally, these methods have not succeeded in producing InP QDs with PL QY and stability comparable to CdSe based QDs. Clearly, other approaches are required.

Here, we present an original approach where an InP core is designed with a specific crystal lattice constant such that it matches the lattice of the shell material. We have developed a simple one-pot method for the synthesis of zinc-blende In_xZn_yP alloy QDs where Zn^{2+} ions are incorporated in the InP structure as substitutional dopants on In^{3+} sites. Depending on the concentration of the Zn precursor added, the lattice constant of the resulting alloy nanocrystals can be tuned from 5.93 Å of the pure InP QDs down to 5.39 Å.

First, we report a comprehensive study of In_xZn_yP alloy QDs encompassing extensive optical, structural, and chemical characterization. Although the addition of Zn to the synthesis of InP nanocrystals has become common practice in the last years,[12−18,22−26] very little has been reported on the actual role of the Zn. The few reports on this topic have focused on the effect on the optical properties, but structural aspects were not investigated.[22,25,31] Here, instead we carry out a detailed investigation on the location of Zn^{2+} in the InP QD lattice. Such compositional tunability is then exploited to match the lattice parameter of the In_xZn_yP cores to that of a range of shell materials (GaP, ZnSe and ZnS) which otherwise would not be compatible with InP. To validate our approach, we synthesized $In_xZn_yP/ZnSe_zS_{1-z}$ core/shell QDs by varying the lattice constants of both core and shell. In all cases, the highest PL QY (up to 60%) was measured when the lattice mismatch was minimum. This demonstrates that the interfacial lattice mismatch is the dominant factor determining the PL QY in these core−shell QDs and that alloying the core to match the shell can effectively alleviate it. Our approach offers significant advantages compared to previous methods, as it allows for a wider range of shell materials to be used. Additionally, it is a straightforward way to increase the quality of InP based QDs, making them suitable candidates for nontoxic LED applications.

RESULTS AND DISCUSSIONS

InP based QDs were prepared following an adaptation of the method described by Kim *et al.*:[7,13] Zn palmitate was added to form In_xZn_yP alloys. The Zn/In precursor ratio was varied between 0 and 20 (see Supporting Information for further details). The resulting particles had a diameter of about 3 nm (Figure 1a); by changing the concentration of Zn, the size of the resulting QDs remained constant within the experimental error (see Figure S1). This could be explained considering that the reactions are carried out with the $P(TMS)_3$ being the limiting precursor.[7] To evaluate the amount of Zn incorporated in the QDs, we performed ICP-OES and XPS analyses on

DOI: 10.1021/acsnano.6b01266
ACS Nano 2016, 10, 4754−4762

carefully washed In_xZn_yP QDs synthesized using different Zn/In ratios (see Experimental Section for details on the washing procedure). Figure 1b clearly shows that when a relatively low amount of Zn precursor (Zn/In feed ratio below 2) is used, a quantitative amount of Zn is detected in the resulting QDs (green dashed line, Figure 1b). A further increase in the Zn/In feed ratio results in an incomplete conversion of the Zn precursor, leading to saturation of the Zn/In ratio around 4 (red dashed line Figure 1b), even when a Zn/In ratio of 20 is used. For this reason, for the remainder of this work we will only discuss samples synthesized with Zn/In feed ratios in the range 0−5.

To determine the location of the Zn atoms in the nanocrystals, the samples were investigated by XRD analysis combined with theoretical modeling (DFT calculations, see Experimental Section for details). The results of the structural characterization are described in Figure 1c−e. The expected crystal structure of InP is shown in Figure 1c (upper panel). The XRD pattern confirms that when no Zn precursor is added to the reaction flask, the phase of the resulting QDs is consistent with that of bulk zinc blende InP (Figure 1d, black pattern). The samples prepared with addition of Zn precursor exhibit the same XRD reflections, but with a systematic shift toward higher diffraction angles as the amount of Zn into the QDs is increased (Figure 1d and Figure S2), which indicates a contraction of the crystal lattice. No other side products, such as Zn_xP_y QDs (*i.e.*, tetragonal or monoclinic Zn_2P, or monoclinic or cubic Zn_3P_2), that would exhibit clear distinct XRD peaks, are observed (see Figure 1d, top panel). Indeed, even cubic Zn_3P_2 exhibits a different crystal structure, as depicted in the sketch of Figure 1c (lower panel). The absence of any Zn_xP_y phase was also supported by a further control experiment we performed: a synthesis was done using only zinc and phosphorus precursors while keeping all the other reaction parameters fixed. This experiment resulted in large nanoparticles with a broad size distribution (diameter of d = 8.3 ± 3.2 nm) (Figure S3). XRD analysis indicated that no phosphides were formed, but a Zn−Si complex with a hememorphite crystal structure was identified. We can exclude that these particles are formed as side product during the synthesis of In_xZn_yP QDs, as the XRD patterns do not show additional peaks of the hememorphite structure, and no large particles are visible in the TEM images of our QDs (Figures S1 and S3). The contraction of the InP lattice upon addition of Zn strongly suggests that Zn atoms are incorporated in the crystal structure, forming In_xZn_yP alloy QDs. We can exclude that Zn^{2+} ions are located only on the surface of the QDs, since in that case no shift of the XRD peaks would be observed.

To identify the position of the Zn ions inside the lattice of the QDs, we performed DFT geometry optimization of small quasi-spherical In_xZn_yP QDs passivated with hydrogen atoms. The fully optimized structure of the QD was then used to compute the XRD reflections (see Experimental Section and Supporting Information for details on the calculations). Three different strategies were adopted to incorporate zinc: (i) only substitutional Zn^{2+} was used; three In^{3+} cations were hence substituted by three Zn^{2+} cations and one P^{3-} anion was removed from the surface of the QD, in order to preserve charge neutrality. (ii) Two Zn^{2+} were substituted onto In^{3+} sites, while a third Zn^{2+} cation was placed at an interstitial position. (iii) Three Zn^{2+} were placed interstitially and two P^{3-} anions were removed from the surface of the QD. We found a strong shift to smaller lattice constants (higher 2θ values) similar to the experimental observation, *only* when considering placing Zn ions substitutionally (strategy (i). In the other scenarios, we either observed a very small shift of the lattice constant (strategy (ii)) or a shift to a larger lattice constant (strategy (iii). Hence, the combination of XRD measurements and DFT calculations suggests that the contraction of the lattice originates from the progressive substitution of indium by zinc ions without introduction of interstitial zinc. The analysis of the bond length inside the QDs structures revealed that the average Zn−P bond length (0.245 nm) was 7.5% smaller than the average In−P bond length (0.265 nm). Furthermore, each substituted Zn atom induced a reduction of the In−P bond length in its direct vicinity (see Supporting Information for details, Figures S4−S9).

XPS analyses further confirmed the formation of In_xZn_yP alloys. XPS is normally considered to be a surface sensitive technique, with a typical penetration depth of up to 10 nm.[32] However, in this case, as our QDs are around 3 nm in diameter, this technique probes the whole QD volume. The reference pure InP QD sample (black spectrum in Figure 2a) shows a In

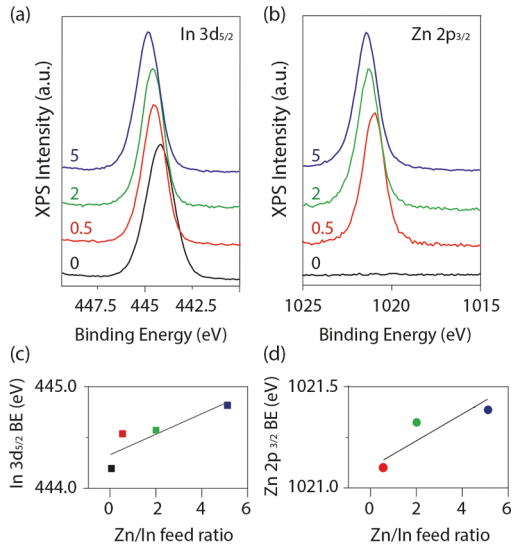

Figure 2. (a and b) In $3d^{5/2}$ and the Zn $2p^{3/2}$ XPS spectra for several In_xZn_yP samples. Each spectrum is labeled with the Zn/In feed ratio. (c and d) The position of In and Zn peaks shifts to higher binding energy values when increasing the Zn/In feed ratio.

$3d_{5/2}$ peak centered at 444.1 ± 0.2 eV, a typical value for In^{3+} compounds.[33−35] By increasing the zinc precursor concentration in the synthesis, a systematic shift of both the In $3d_{5/2}$ (Figure 2a) and the Zn $2p_{3/2}$ (Figure 2b) peaks to higher binding energies is observed. The In $3d_{5/2}$ peak shifts up to 444.8 ± 0.2 eV, for Zn/In = 5, still consistent with a 3+ oxidation state.[30] The Zn $2p_{3/2}$ peak shifts from 1021.1 ± 0.2 eV, for Zn/In = 0.5, to 1021.4 ± 0.2 eV, for Zn/In = 5. Even though the Zn $2p_{3/2}$ peak energies are close to those reported for Zn(II) phosphides,[30] the observed trends (Figure 2c,d) are not consistent with the growth of a Zn-based phosphide shell as in that case the local In environment would not have changed and the In peaks would not have shifted. In line with previous work on alloyed QDs[36,37] and in accordance with the XRD results, the fact that *both* In and Zn XPS peaks shift as the Zn/In ratio increases is interpreted as the modification of the chemical environment experienced by *both* In^{3+} and Zn^{2+} ions, as a consequence of the formation of an In_xZn_yP alloy structure.

DOI: 10.1021/acsnano.6b01266
ACS Nano 2016, 10, 4754−4762

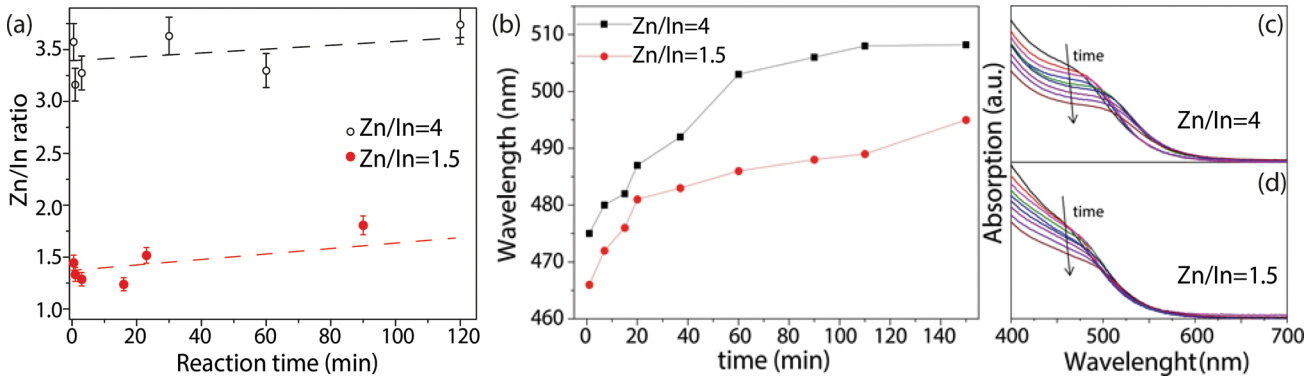

Figure 3. (a) Plot of the Zn/In ratios measured using ICP- OES at different stages of the reaction for In_xZn_yP for Zn/In feed ratios of 1.5 (red full dots) and 4 (black empty dots). (b) Plot of the peak absorption wavelength against time for a In_xZn_yP QD synthesis with Zn/In = 4 (black curve) and Zn/In = 1.5 (red curve). (c and d) Evolution of the absorption spectra over time during the reaction for In_xZn_yP with (c) Zn/In = 4 and (d) Zn/In = 1.5.

Moreover, quantitative XPS analysis (shown as red squares in Figure 1b) confirms the Zn/In values obtained by ICP-OES: as discussed in ref 42 and in ref 37 in the case of core/shell QDs, XPS would have been affected by the layered structure of the system. The agreement between XPS and ICP-OES results therefore strongly supports the formation of an In_xZn_yP alloy structure.

A kinetic study of the synthesis was carried out in order to understand the formation mechanism of In_xZn_yP alloy QDs. We monitored *via* ICP-OES the Zn/In ratio at different stages of the reaction (between 30 s and 2 h) for Zn/In = 1.5 and Zn/In = 4 feed ratios (Figure 3a). Two possible pathways were considered: (i) after the nucleation and growth of InP QDs, In^{3+} is replaced by Zn^{2+} *via* a cation exchange reaction;[38,39] or (ii) In^{3+} and Zn^{2+} react simultaneously with P^{3-} directly forming alloyed In_xZn_yP QDs. In scenario (i), we expect to see a significant increase in Zn^{2+} content at a certain stage during the reaction. The observed Zn/In ratio was roughly constant during the whole reaction, showing a slight variation from 1.45 to 1.80 in the case of Zn/In = 1/5, and from 3.56 to 3.73 in the case of Zn/In = 4. Absorption measurements (Figures 3b–d) confirmed that the QDs were growing during the whole period shown in Figure 3b. The results suggest that In^{3+} and Zn^{2+} react simultaneously with P^{3-} to form In_xZn_yP (scenario (ii)), as the Zn/In ratio remains constant during the reaction, ruling out any postnucleation cation exchange process. Additionally, this further indicates that the formation of a core/shell structure is unlikely, as in that case we would have observed a situation similar to the one described in scenario (i).

The In_xZn_yP alloy bulk structure has not been reported to date, and the pure materials ($x = 0$ and $y = 0$, *i.e.*, InP, Zn_3P_2, or Zn_2P) have different crystal structure (Figure 1d). However, our results demonstrate that a metastable cubic phase of In_xZn_yP alloy can exist at the nanocrystal level. This is not completely surprising because zinc phosphide can crystallize in a cubic Zn_3P_2 phase in which the anion framework is almost identical to that of InP.[40−42] Both structures exhibit an almost identical FCC phosphorus sublattice (with a P−P bonds length of 4.02 Å for Zn_3P_2, and 4.15 Å for InP) where the cations occupy tetrahedral sites (see sketch in Figures 1c and S10). The isomorphism of these two structures suggests that an alloy can form.

An important aspect to consider is the charge of the In_xZn_yP alloy QDs. As argued above, the alloyed structure is formed when In^{3+} is replaced with Zn^{2+} creating a charge imbalance. However, we estimated the net charge in our QDs using ζ-potential measurements (see Supporting Information for details), and the results (depicted in Figure S11) indicate that for all samples the charge is zero within the experimental error, suggesting that a net balancing of the charges occurred during the formation of such alloys. We can envisage four charge compensating scenarios: (i) p-doping could occur to compensate for the net negative charge. However, this would most likely lead to efficient Auger quenching and an absorption bleach,[43] of which we found no indications in the UV−vis absorption and emission measurements (see Figure 4a below). (ii) Zn^{2+} could occupy both interstitial and substitutional positions in the NC: in this case, every three Zn^{2+} incorporated in the NCs only two In^{3+} sites would be occupied, preserving neutrality. A comparison between experimental and simulated XRD patterns presented above suggests that this scenario is

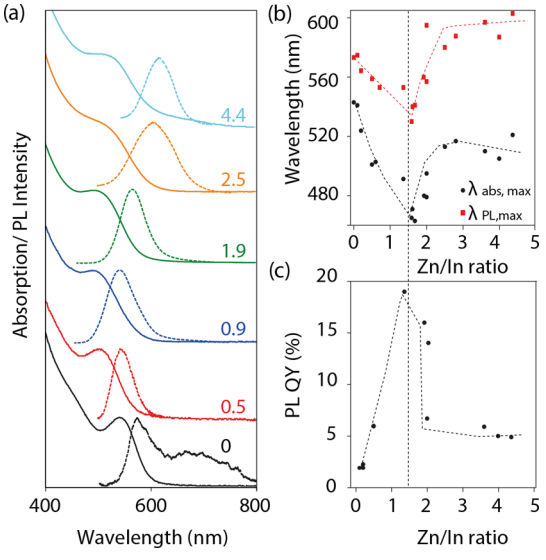

Figure 4. (a) Normalized absorption and PL spectra of In_xZn_yP QDs. Except for a variable Zn/In ratio, all other synthesis conditions were identical. (b) Plot of $\lambda_{Abs,max}$ (nm) for the absorption (black dots) and PL emission (red squares) wavelengths as a function of the Zn/In molar ratio obtained by ICP(OES) analysis. Dashed lines represent a guide to the eye. (c) Plot of the PL QY (%) of In_xZn_yP QDs as a function of the Zn/In molar ratio obtained by ICP(OES) elemental analysis.

DOI: 10.1021/acsnano.6b01266
ACS Nano 2016, 10, 4754−4762

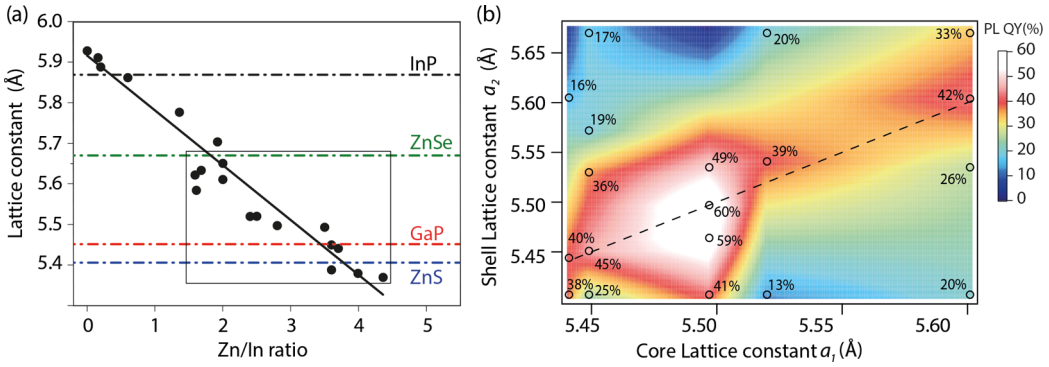

Figure 5. (a) Plot of the lattice constant of In_xZn_yP QDs as a function of the Zn/In measured ratio. Dashed lines indicate the lattice constants of bulk InP (black ICSD code 24517), ZnSe (green ICSD code 77091), GaP (red ICSD code 77087), and ZnS (blue ICSD code 60378). (b) Color plot of the PL QY as a function of the lattice constant of the $ZnSe_zS_{1-z}$ shell a_2 and the lattice constant of the core a_1. The data points (black empty dots) were interpolated with a linear fit. The dashed line indicates lattice matching between core and shell ($a_1 = a_2$).

improbable. (iii) Negatively charged x-type palmitate ligands could desorb from the surface to preserve the charge.[44] At present, we have no evidence in favor or against this scenario. (iv) Phosphorus vacancies could form to balance the charge (one for every three In^{3+} replaced by three Zn^{2+}). This hypothesis has already been taken into consideration in the DFT calculations described above, and therefore, it appears likely.

To decide if scenario (iv) applies to our QDs, we carried out TEM-EDX analysis to determine the In/Zn/P ratios (see Supporting Information for details and Table S1). Three different In_xZn_yP samples with Zn/In ratios of 0, 0.3, and 1.3 were analyzed. As more zinc is added to the QDs, the amount of phosphorus decreases from 27% (pure InP) to 19% (Zn/In = 1.3), in line with the formation of phosphorus vacancies. However, the decrease in phosphorus does not keep up with the amount of zinc added. A tentative explanation for this observation is that a fraction of the zinc atoms (roughly 1/3 based on the charge balance with phosphorus) is included in the crystal lattice, while the remaining fraction is localized at the surface of the QDs.

The inclusion of zinc inside the InP lattice does not only influence the structure of the resulting QDs, but also their optical properties. Figure 4a shows the absorption (solid line) and the PL emission (dashed line) of In_xZn_yP QDs with different Zn/In ratios. The variation of the exciton absorption peak maximum ($\lambda_{Abs,max}$, black dots) and the PL maximum ($\lambda_{PL,max}$, red dots) *versus* the Zn/In ratio measured with ICP-OES are shown in Figure 4b. By increasing the concentration of zinc up to 1.5, a systematic blue-shift of both $\lambda_{Abs,max}$ and $\lambda_{PL,max}$ was observed, while after further incorporation of Zn^{2+} (*i.e.*, for Zn/In > 1.5), the trend reversed and a red-shift of the optical features was observed. A possible explanation for the blue shift could be that the presence of Zn-carboxylates in the reaction mixture influences the kinetics of the reaction, leading to smaller particles.[22,25] However, TEM measurements indicated that In_xZn_yP QDs having different Zn concentrations have comparable sizes (see Figure S1). An alternative explanation is that the alloyed In_xZn_yP material has a different (bulk) bandgap than pure InP.[21] Indeed, it is well-known that in many bulk semiconductor alloys there is a direct correlation between the alloy composition and its band gap.[45−49] In addition, the degree of quantum confinement could also be different, if the effective masses of electrons and holes change in the alloy. These combined effects could result in the strongly nonlinear trends observed in Figure 4b. Interestingly, a variation in Zn content does not affect the full width half-maximum (fwhm) of the PL emission, which is roughly constant (see Table S2).

As previously reported, the addition of zinc precursor has a clear influence on the removal of trap states.[22,25] While the PL emission spectrum of the pure InP QDs (Figure 4a black curve) is characterized by a broad secondary peak at lower energies, usually assigned to defect emission,[50,51] this peak was suppressed upon the introduction of zinc, as has been previously observed by Thuy *et al.*[22] At the same time, the PL QY of the alloyed QDs increased from about 0−1% in pure InP up to 20% for Zn/In = 1.5 (Figure 4c) and the PL decay became longer (see Figure S12 and Table S3), suggesting that the Zn^{2+} ions, in addition to being incorporated in the QD lattice, could passivate the surface of the QDs.[22,52,53]

The possibility of tuning both optical properties and lattice parameters of the In_xZn_yP QDs by varying only one synthetic parameter, *i.e.*, the amount of Zn precursor, is promising for achieving high PL QY QDs upon the epitaxial growth of a lattice-matching shell material. Depending on the amount of zinc incorporated, the lattice constants of the QDs, which were calculated from the corresponding XRD patterns using a Nelson-Riley plot,[54,55] can be tuned linearly from 5.93 Å, in the case of pure InP, to 5.39 Å for In_xZn_yP with Zn/In = 4.4 (Figure 5a). This range spans the lattice constants of most commonly used shell materials, like ZnSe (a = 5.66 Å),[30] GaP (a = 5.45 Å),[29] and ZnS (a = 5.42 Å),[30] which all have the same zinc blende crystal structure and have suitable type-I band offsets. Our approach therefore offers a simple way to overcome the problem of the lattice mismatch in core/shell structures.

As a proof of concept, we synthesized five different In_xZn_yP cores by varying the Zn/In ratio, in order to obtain QDs with different lattice constants: Zn/In = 2.0 (a = 5.60 Å), Zn/In = 2.4 (a = 5.52 Å), Zn/In = 2.8 (a = 5.49 Å), Zn/In = 3.7 (a = 5.45 Å), and Zn/In = 3.6 (a = 5.44 Å). For each core, we grew a $ZnSe_zS_{1-z}$ shell varying the shell composition from ZnSe (z = 1) to ZnS (z = 0) (see Experimental Section and Supporting Information for details) and, thus, the corresponding lattice parameters. $ZnSe_zS_{1-z}$ is a well-known alloy whose lattice parameters are reported in literature and can be finely tuned from 5.67 Å for z = 1 to 5.41 Å for z = 0 (see Figure S13a) varying the material's composition.[30] A calibration curve of the shell lattice constant as a function of z is constructed from literature data and shown in Figure S13 of the Supporting Information. The Se and S fractions in the core/shell samples

DOI: 10.1021/acsnano.6b01266
ACS Nano 2016, 10, 4754−4762

were determined by ICP (OES) and the results are given in Table S4. From these results, the value of z is extracted and used to calculate the lattice constants of the $ZnSe_zS_{1-z}$ shells, using the calibration curve (Figure S13b). Figure S14 shows the absorption and emission spectra of the $In_xZn_yP/ZnSe_zS_{1-z}$ core/shell, and the relative TEM images. The resulting core/shell QDs have a shell thickness of 0.6 nm which roughly correspond to 1 ML of $ZnSe_zS_{1-z}$.

Figure 5b shows a 2D plot of the PL QY (color scale) *versus* the lattice constant of the core a_1 (x-axis) and the lattice constant of the shell a_2 (y-axis). The dashed line indicates lattice matching between core and shell (see also Figure S13b). For each different In_xZn_yP core, the highest PL QY value (up to 60%) was recorded when the lattice mismatch was minimum. These results demonstrate that interfacial lattice mismatch is the dominant cause of a low PL QY in these core−shell QDs and that it can be reduced significantly by designing the core crystal structure with specific lattice spacing. The overall PL QY is highest for In_xZn_yP cores with a Zn/In ratio of 2.8 and a matching $ZnSe_zS_{1-z}$ shell with a = 5.49 Å. However, not for every starting core the PL reaches the same maximum, which suggests that in addition to core/shell lattice matching, other parameters also play a role. Table S5 in the Supporting Information compares the PL QY of the initial core with the QY of the respective core/shell QDs. We observe that the highest PL QY (60%) measured for a core/shell was achieved with the brightest cores (QY = 12%). Possibly, the initial quality of the core plays an important role in the overall efficiency of the resulting core/shell structure. This suggests that surface defects, or even local surface oxidation, could be retained as interface defects in the core−shell structures. Still, it is clear that for any core composition the QY of the resulting core/shell QDs can only be high for fully matched core and shell lattices.

CONCLUSIONS

In summary, we have presented an approach to overcome the problem of the lattice mismatch in InP based core/shell structures. We developed a method to design the core crystal structure with specific lattice spacing such that it matches the lattice of different shell materials. This is achieved by alloying InP with Zn^{2+} ions, leading to luminescent In_xZn_yP QDs whose lattice constant can be finely tuned by varying the concentration of Zn, and the composition of the In_xZn_yP alloy nanocrystals could be tuned up to a Zn/In ratios as high as 20. A combination of XRD, ICP-OES, and XPS results, combined with DFT modeling, showed that Zn^{2+} is included as a substitutional dopant on In^{3+} sites producing a systematic contraction of the crystal lattice. The possibility of tuning the lattice constant of the In based QDs expands the range of shell materials compatible with InP. Additionally, we demonstrated that the PL QY is highest when the lattices parameters of core and shell are matched, such that a maximum PL QY of 60% could be achieved in the core/shell nanocrystals. Our method represents a simple and effective way to alleviate lattice mismatch in core/shell QDs, paving the way for the fabrication of defect free QD heterostructures.

EXPERIMENTAL SECTION

Materials. Indium(III) acetate ($In(OAc)_3$, 99.99%), palmitic acid (PA, $C_{15}H_{31}COOH$, 99.99%, stored at −20 °C), tris(trimethylsilyl)-phosphine ($P(SiMe_3)_3$, 95%), zinc(II) acetate ($Zn(OAc)_2$, 99.99%), ammonium sulfide solution ($S(NH_4)_2$, 20% in H_2O), 1-octadecene (ODE, 95%) formamide (FA, 99%), dimethylformamide (DMF, 99%), Zn stearate (technical grade), sulfur powder (99.98% trace metals basis), and trioctylphosphine (TOP, 90% technical grade) were purchased from Sigma-Aldrich. Selenium powder (99.98% trace metals basis) was purchased by Chem Pure. All the chemicals were used without further purification.

Synthesis of In_xZn_yP Core QDs.[7,13] In a typical synthesis using a Zn/In molar ratio of 1, in a three-neck flask were mixed 35 mg of $In(OAc)_3$ (0.12 mmol), 11 mg of $Zn(OAc)_2$ (0.06 mmol), and 91 mg of palmitic acid (0.36 mmol) in 7 mL of ODE. The solution was degassed under vacuum for 1 h at 140 °C. After heating the solution to 300 °C under nitrogen flow, 17 μL of $(P(TMS)_3)$ (0.06 mmol; 15 mg) in 1 mL of ODE was rapidly injected. The temperature was then lowered to 270 °C and held for 2 h. The In_xZn_yP NCs were washed three times by dispersion in toluene followed by precipitation by addition of a mixture of ethanol/acetone (1:3), and stored in toluene or hexane in a N_2 filled vial in the glovebox. The amount of zinc precursors was varied between 0 mg (for Zn/In = 0) and 220 mg (for Zn/In = 10), while the $In(OAc)_3$ and $P(TMS)_3$ were kept constant.

Synthesis of Zn_xP_y Core QDs. Zn_xP_y nanoparticles were synthesized following the method described above for In_xZn_yP QDs, without addition of $In(OAc)_3$ in the reaction mixture. Zn/P ratios of 1 and 2 were used.

Synthesis of $In_xZn_yP/ZnSe_zS_{z-1}$ Core/Shell QDs.[12] For a typical synthesis, 0.325g of Zn stearate in 1.5 mL of ODE was added into a three next flask containing 2 mL of as synthesized In_xZn_yP cores at room temperature. Separately, a 1 M stock solution of TOP-Se was prepared by dissolving 4 mmol of Se powder in 4 mL of TOP. A 1 M TOP-S stock solution was prepared with the same procedure as TOP-Se. Upon addition of the Zn precursor, the temperature of the reaction mixture was set to 300 °C with a heating rate of 10 °C/min. When the temperature was about 90 °C, a total of 0.5 mL of the anion stock solution (Se-TOP + S-TOP) was added. The $ZnSe_zS_{z-1}$ composition was changed by varying the Se-TOP and S-TOP precursor amount: for example, in case of z = 0, 0.5 mL of 1 M TOP-S was added, while in case of z = 0.5, 0.25 mL of 1 M TOP-Se and 0.25 mL of 1 M TOP-S were added. We verified by ICP-OES measurements that the Se/S ratio in the shell matches the Se/S precursor ratio (see Table S3). The reaction was kept at 300 °C for 20 min, and subsequently quenched by lowering the temperature. The product was purified by dispersion in chloroform (2 mL) followed by precipitation by addition of a mixture of ethanol/acetone (1:4). The obtained particles were stored in toluene in a N_2 filled vial in the glovebox.

Ligand Exchange.[56] A colloidal dispersion of washed NCs with organic ligands was prepared in nonpolar solvents like toluene, while the solution of inorganic ligands was prepared in polar formamide (FA), which is immiscible with toluene. The exchange of inorganic ligand with S^{2-} was carried out in a N_2 glovebox. A volume of 20 μL of $(NH_4)_2S$ solution was added to 1 mL of FA and mixed with 1 mL of a NC dispersion in toluene. The mixture was sonicated for 15 min in a sonic bath at 60 °C, leading to a complete phase transfer of the NCs from toluene to the FA phase. The phase transfer can be easily monitored by the color change of toluene (red to colorless) and FA (colorless to red) phases. The FA phase was separated and acetone was added as nonsolvent to precipitate the particles. To remove any remaining nonpolar organic ligand, a further washing step with toluene as a nonsolvent was applied. This was repeated twice. The QDs were then dispersed in dimethylformamide (DMF) for further analysis and stored in a N_2 filled vial in the glovebox.

Characterization. *Absorption and Emission UV−Vis Measurements.* QD samples for optical analysis were prepared by diluting the stock solutions in toluene in a 1 cm quartz cuvette. Absorption spectra were measured on the PerkinElmer L900 and L40 UV/vis spectrometers. Emission spectra were obtained using a PTI Quanta-Master with a 75 W xenon lamp, using an excitation wavelength at 400 nm.

Absolute QY Measurements. QD samples for PL QY measurements were prepared by diluting the purified stock solutions in toluene. PL quantum yields (QY) were determined using an integrated sphere setup at Philips Research Laboratory. The setup consisted of a

DOI: 10.1021/acsnano.6b01266
ACS Nano 2016, 10, 4754−4762

445 nm diode laser, a Labsphere 6″ integrating sphere and a fiber coupled spectrometer (USB 4000, Ocean Optics). The combination of sphere, fiber and spectrometer was calibrated with a light source of known emission characteristics.

Time-Resolved PL Measurements. QD samples were prepared by diluting the stock solutions in toluene in a 1 cm quartz cuvette. PL lifetimes were recorded using an Edinburgh LifeSpec spectrometer equipped with a single photon counter. The samples were excited at 405 nm with a picosecond pulsed diode laser (Hamamatsu, M8903-01, $I_0 = 4 \times 10^{12}$ photons/cm^2).

Transmission Electron Microscopy (TEM), Scanning Transmission Electron Microscopy (STEM), and Energy Dispersive X-ray (EDX) Spectroscopy. Samples for analysis were obtained by dipping carbon coated copper TEM grids in the NPs solution and blotting on a filter paper at room temperature. TEM images and elemental analysis were obtained with a Philips CM30, INCA x-sight operating at 120 eV. A Tecnai G2 F20 transmission electron microscope, equipped with a Schottky gun operated at 200 kV acceleration voltage, was used to acquire high angle annular dark field (HAADF)-scanning TEM (STEM) images of the samples.

Inductively Coupled Plasma (ICP) Optical Emission Spectroscopy (OES) Elemental Analysis. ICP measurements were carried out using a iCAP 6500 Thermo spectrometer. All chemical analyses performed by ICP-OES were affected by a systematic error of about 5%. Samples were dissolved in HCl/HNO_3 3:1 (v/v).

X-ray Photoelectron Spectroscopy (XPS). Samples for XPS were prepared by drop-casting a solution of NCs onto silicon wafers. XPS measurements were performed on a Kratos Axis Ultra DLD spectrometer, using a monochromatic Al Kα source operating at 15 kV and 20 mA. Wide scans were acquired at analyzer pass energy of 160 eV, while high resolution narrow scans were performed at constant pass energy of 10 eV and steps of 0.1 eV. The photoelectrons were detected at a takeoff angle $\Phi = 0°$ with respect to the surface normal. The pressure in the analysis chamber was maintained below 5×10^{-9} Torr for data acquisition. The data were converted to VAMAS format and processed using CasaXPS software, version 2.3.16. The binding energy (BE) scale was internally referenced to the C 1s peak (BE for C−C = 284.8 eV).

Powder X-ray Diffraction Patterns (XRD). Specimens for the XRD measurements were prepared in a glovebox by dropping a concentrated NCs solution onto a quartz zero-diffraction single crystal substrate. XRD measurements were performed on a PANanalytical Empyrean X-ray diffractometer equipped with a 1.8 kW Cu Kα ceramic X-ray tube, PIXcel3D 2 × 2 area detector and operating at 45 kV and 40 mA. The diffraction patterns were collected in air at room temperature using Parallel-Beam (PB) geometry and symmetric reflection mode. XRD data analysis was carried out using HighScore 4.1 software from PANalytical.

Calculation of Lattice Parameters. To calculate the lattice constant of the measured QDs, Nelson-Riley plots were made (using the three reflections in the 2θ scans) to determine the In_xZn_yP lattice parameters, as shown in Figure 1d. The uncertainty is on the order of 10^{-2} Å, which is defined by z-position accuracy, 2θ step size, and the slope of Nelson-Riley plots.[47,54,55] The position of the three reflections was obtained by fitting the diffraction peaks with a Gaussian function using Origin Pro 9.0. Note that the Nelson-Riley method minimizes systematic error contributions to the uncertainty on the quoted lattice parameters, as reported in references.[47,54,55]

Electrophoresis Measurements. The charge of the synthesized In_xZn_yP QDs was determined through measurement of the electrophoretic mobility. A total of 750 μL of a diluted QDs solution in toluene was loaded into the Malvern PCS1115 nonaqueous dip cell and measured on Malvern Zetasizer Z Nano operating at 25 °C. The electrophoretic mobility μ_e was converted to the ζ-potential using the Hückel approximation, averaged over three measurements, according to

$$\zeta = \frac{1.5\eta\mu_e}{\varepsilon\varepsilon_0}$$

Here, the viscosity η and the dielectric constant ε depend on the type of solvent (toluene).

Theoretical Calculations. Initial geometries of quasi-spherical stoichiometric InP NCs were generated using a home-built software and assuming the bulk crystal structure. The dangling bonds of the resulting quantum dots were passivated with hydrogen atoms. Hydrogen atoms were here preferred to organic surfactant molecules to ease the calculations. The scripts used to generate these initial geometries are available upon demand. Zinc atoms were then incorporated in the composition of these InP NCs following three different methods. In the first method, three Zn atoms (oxidation state +2) replaced 3 In (oxidation state +3) atoms in the lattice. To compensate the charges, 1 phosphorus atom (oxidation state −3) was removed at the surface of the NCs. In the second approach, only 2 Zn atoms replaced 2 In atoms and one additional Zn atom was introduced as an interstitial dopant to balance the charge. These two approaches were then iterated to obtain Zn/In ratio close to unity. The geometries of the resulting NCs were then fully relaxed at the density functional level of theory (DFT). The Amsterdam Density Functional (ADF) package was used to perform these geometry optimizations.[57−59] Due to some difficulties encountered during the electronic structure calculation in some systems, a large threshold of $1e^{-4}$ was used to stop the SCF cycles and a charge smearing up to 0.01 hartree was employed. A scalable SCF approach was employed to accelerate the calculations. The simulations of the XRD spectra were done using the debyer software.[59] An X-ray wavelength of 0.154 nm was used in agreement with the copper source used experimentally.

ASSOCIATED CONTENT

Supporting Information

The Supporting Information is available free of charge on the ACS Publications website at DOI: 10.1021/acsnano.6b01266.

Experimental details and additional figures (PDF)

AUTHOR INFORMATION

Corresponding Author

*E-mail: f.pietra@tudelft.nl.

Notes

The authors declare no competing financial interest.

ACKNOWLEDGMENTS

The authors thank Dr. Wiel H. Evers for assistance with TEM analysis. This research is supported by the Dutch Technology Foundation STW, which is part of The Netherlands Organization for Scientific Research (NWO), and which is partly funded by Ministry of Economic Affairs; by the 7th European Community Framework Programme under Grant Agreement No. 614897 (ERC Consolidator Grant "TRANS-NANO"), Grant Agreement No. 240299 (ERC Consolidator Grant "SING FISS"); and by the ERC Horizon 2020 under the Grant Agreement No. 648433(ICONICAL).

REFERENCES

(1) De Mello Donegá, C. Synthesis and Properties of Colloidal Heteronanocrystals. *Chem. Soc. Rev.* **2011**, *40*, 1512−1546.

(2) Reiss, P.; Protière, M.; Li, L. Core/Shell Semiconductor Nanocrystals. *Small* **2009**, *5*, 154−168.

(3) Mashford, B. S.; Stevenson, M.; Popovic, Z.; Hamilton, C.; Zhou, Z.; Breen, C.; Steckel, J.; Bulovic, V.; Bawendi, M.; Coe-Sullivan, S.; Kazlas, P. T. High-Efficiency Quantum-Dot Light-Emitting Devices with Enhanced Charge Injection. *Nat. Photonics* **2013**, *7*, 407−412.

(4) Zhang, Q.; Wang, C.-F.; Ling, L.-T.; Chen, S. Fluorescent Nanomaterial-Derived White Light-Emitting Diodes: What's Going on. *J. Mater. Chem. C* **2014**, *2*, 4358−4373.

DOI: 10.1021/acsnano.6b01266
ACS Nano 2016, 10, 4754−4762

(5) Chen, O.; Zhao, J.; Chauhan, V. P.; Cui, J.; Wong, C.; Harris, D. K.; Wei, H.; Han, H.-S.; Fukumura, D.; Jain, R. K.; Bawendi, M. Compact High-Quality CdSe-CdS Core-Shell Nanocrystals with Narrow Emission Linewidths and Suppressed Blinking. *Nat. Mater.* **2013**, *12*, 445−451.
(6) Boldt, K.; Kirkwood, N.; Beane, G. A.; Mulvaney, P. Synthesis of Highly Luminescent and Photo-Stable, Graded Shell CdSe/$Cd_XZn_{1-X}S$ Nanoparticles by In Situ Alloying. *Chem. Mater.* **2013**, *25*, 4731−4738.
(7) Battaglia, D.; Peng, X. Formation of High Quality InP and InAs Nanocrystals in a Noncoordinating Solvent. *Nano Lett.* **2002**, *2*, 1027−1030.
(8) Xie, R.; Battaglia, D.; Peng, X. Colloidal InP Nanocrystals as Efficient Emitters Covering Blue to near-Infrared. *J. Am. Chem. Soc.* **2007**, *129*, 15432−15433.
(9) Soenen, S. J.; Manshian, B. B.; Aubert, T.; Himmelreich, U.; Demeester, J.; De Smedt, S. C.; Hens, Z.; Braeckmans, K. Cytotoxicity of Cadmium-Free Quantum Dots and Their Use in Cell Bioimaging. *Chem. Res. Toxicol.* **2014**, *27*, 1050−1059.
(10) Mushonga, P.; Onani, M. O.; Madiehe, A. M.; Meyer, M. Indium Phosphide-Based Semiconductor Nanocrystals and Their Applications. *J. Nanomater.* **2012**, *2012*, 1−11.
(11) Yang, X.; Zhao, D.; Leck, K. S.; Tan, S. T.; Tang, Y. X.; Zhao, J.; Demir, H. V.; Sun, X. W. Full Visible Range Covering InP/ZnS Nanocrystals with High Photometric Performance and Their Application to White Quantum Dot Light-Emitting Diodes. *Adv. Mater.* **2012**, *24*, 4180−4185.
(12) Lim, J.; Bae, W. K.; Lee, D.; Nam, M. K.; Jung, J.; Lee, C.; Char, K.; Lee, S. InP@ZnSeS, Core@Composition Gradient Shell Quantum Dots with Enhanced Stability. *Chem. Mater.* **2011**, *23*, 4459−4463.
(13) Kim, S.; Kim, T.; Kang, M.; Kwak, S. K.; Yoo, T. W.; Park, L. S.; Yang, I.; Hwang, S.; Lee, J. E.; Kim, S. K.; Kim, S.-W. Highly Luminescent InP/GaP/ZnS Nanocrystals and Their Application to White Light-Emitting Diodes. *J. Am. Chem. Soc.* **2012**, *134*, 3804−3809.
(14) Kim, T.; Kim, S. W.; Kang, M.; Kim, S.-W. Large-Scale Synthesis of InPZnS Alloy Quantum Dots with Dodecanethiol as a Composition Controller. *J. Phys. Chem. Lett.* **2012**, *3*, 214−218.
(15) Kim, K.; Lee, H.; Ahn, J.; Jeong, S. Highly Luminescing Multi-Shell Semiconductor Nanocrystals InP/ZnSe/ZnS. *Appl. Phys. Lett.* **2012**, *101*, 073107.
(16) Li, L.; Reiss, P. One-Pot Synthesis of Highly Luminescent InP/ZnS Nanocrystals without Precursor Injection. *J. Am. Chem. Soc.* **2008**, *130*, 11588−11589.
(17) Lim, J.; Park, M.; Bae, W. K.; Lee, D.; Lee, S.; Lee, C.; Char, K. Highly Efficient Cadmium-Free Quantum Dot Light-Emitting Diodes Enabled by the Direct Formation of Excitons within InP@ZnSeS Quantum Dots. *ACS Nano* **2013**, *7*, 9019−9026.
(18) Mutlugun, E.; Hernandez-Martinez, P. L.; Eroglu, C.; Coskun, Y.; Erdem, T.; Sharma, V. K.; Unal, E.; Panda, S. K.; Hickey, S. G.; Gaponik, N.; Eychmüller, A.; Demir, H. V. Large-Area (over 50 Cm × 50 Cm) Freestanding Films of Colloidal InP/ZnS Quantum Dots. *Nano Lett.* **2012**, *12*, 3986−3993.
(19) Kim, K.; Han, C.-S.; Jeong, S. Design and Synthesis of Photostable Multi-Shell Cd-Free Nanocrystal Quantum Dots for LED Applications. *J. Mater. Chem.* **2012**, *22*, 21370−21372.
(20) Tessier, M. D.; Dupont, D.; De Nolf, K.; De Roo, J.; Hens, Z. Economic and Size-Tunable Synthesis of InP/ZnE (E = S,Se) Colloidal Quantum Dots. *Chem. Mater.* **2015**, *27*, 4893−4898.
(21) Kim, S.; Park, J.; Kim, T.; Jang, E.; Jun, S.; Jang, H.; Kim, B.; Kim, S.-W. Reverse Type-I ZnSe/InP/ZnS Core/shell/shell Nanocrystals: Cadmium-Free Quantum Dots for Visible Luminescence. *Small* **2011**, *7*, 70−73.
(22) Thuy, U. T. D.; Reiss, P.; Liem, N. Q. Luminescence Properties of In(Zn)P Alloy core/ZnS Shell Quantum Dots. *Appl. Phys. Lett.* **2010**, *97*, 193104.
(23) Song, W.-S.; Lee, H.-S.; Lee, J. C.; Jang, D. S.; Choi, Y.; Choi, M.; Yang, H. Amine-Derived Synthetic Approach to Color-Tunable InP/ZnS Quantum Dots with High Fluorescent Qualities. *J. Nanopart. Res.* **2013**, *15*, 1750.
(24) Xi, L.; Cho, D.-Y.; Duchamp, M.; Boothroyd, C. B.; Lek, J. Y.; Besmehn, A.; Waser, R.; Lam, Y. M.; Kardynal, B. Understanding the Role of Single Molecular ZnS Precursors in the Synthesis of In(Zn)P/ZnS Nanocrystals. *ACS Appl. Mater. Interfaces* **2014**, *6*, 18233−18242.
(25) Xu, S.; Ziegler, J.; Nann, T. Rapid Synthesis of Highly Luminescent InP and InP/ZnS Nanocrystals. *J. Mater. Chem.* **2008**, *18*, 2653−2656.
(26) Ryu, E.; Kim, S.; Jang, E.; Jun, S.; Jang, H.; Kim, B.; Kim, S.-W. Step-Wise Synthesis of InP/ZnS Core−Shell Quantum Dots and the Role of Zinc Acetate. *Chem. Mater.* **2009**, *21*, 573−575.
(27) Peng, X.; Schlamp, M. C.; Kadavanich, A. V.; Alivisatos, A. P. Epitaxial Growth of Highly Luminescent CdSe/CdS Core/Shell Nanocrystals with Photostability and Electronic Accessibility. *J. Am. Chem. Soc.* **1997**, *119*, 7019−7029.
(28) Hollingsworth, J. A. Heterostructuring Nanocrystal Quantum Dots Toward Intentional Suppression of Blinking and Auger Recombination. *Chem. Mater.* **2013**, *25*, 1318−1331.
(29) Rabadanov, M. K.; Loshmanov, A. A.; Shaldin, Y. V. Anharmonic Thermal Vibrations of Atoms in Crystals with Sphalerite Structure-GaP, ZnS, ZnSe, and ZnTe: High-Temperature X-Ray Structure Studies. *Crystallogr. Rep.* **1997**, *42*, 592−602.
(30) Sadekar, H. K.; Ghule, A. V.; Sharma, R. Bandgap Engineering by Substitution of S by Se in Nanostructured $ZnS_{1-x}Se_x$ Thin Films Grown by Soft Chemical Route for Nontoxic Optoelectronic Device Applications. *J. Alloys Compd.* **2011**, *509*, 5525−5531.
(31) Mordvinova, N. E.; Vinokurov, A. A.; Lebedev, O. I.; Kuznetsova, T. A.; Dorofeev, S. G. Addition of Zn during the Phosphine-Based Synthesis of Indium Phospide Quantum Dots: Doping and Surface Passivation. *Beilstein J. Nanotechnol.* **2015**, *6*, 1237−1246.
(32) Hoener, C. F.; Allan, K. A.; Bard, A. J.; Campion, A.; Fox, M. A.; Mallouk, T. E.; Webber, S. E.; White, J. M. Demonstration of a Shell-Core Structure in Layered Cadmium Selenide-Zinc Selenide Small Particles by X-Ray Photoelectron and Auger Spectroscopies. *J. Phys. Chem.* **1992**, *96*, 3812−3817.
(33) NIST X-ray Photoelectron Spectroscopy Database, Version 4.1 (National Institute of Standards and Technology, Gaithersburg, 2012; http://srdata.nist.gov/xps/.
(34) Faur, M.; Faur, M.; Jayne, D. T.; Goradia, M.; Goradia, C. XPS Investigation of Anodic Oxides Grown on P-Type InP. *Surf. Interface Anal.* **1990**, *15*, 641−650.
(35) Kazmerski, L. L. Comparison of Low-Temperature Oxides on Polycrystalline InP by AES, SIMS, and XPS. *J. Vac. Sci. Technol.* **1980**, *17*, 1061.
(36) De Trizio, L.; Prato, M.; Genovese, A.; Casu, A.; Povia, M.; Simonutti, R.; Alcocer, M. J. P.; D'Andrea, C.; Tassone, F.; Manna, L. Strongly Fluorescent Quaternary Cu−In−Zn−S Nanocrystals Prepared from $Cu_{1-X}InS_2$ Nanocrystals by Partial Cation Exchange. *Chem. Mater.* **2012**, *24*, 2400−2406.
(37) Akkerman, Q. A.; Genovese, A.; George, C.; Prato, M.; Moreels, I.; Casu, A.; Marras, S.; Curcio, A.; Scarpellini, A.; Pellegrino, T.; Manna, L.; Lesnyak, V. From Binary Cu2S to Ternary Cu-In-S and Quaternary Cu-In-Zn-S Nanocrystals with Tunable Composition *via* Partial Cation Exchange. *ACS Nano* **2015**, *9*, 521−531.
(38) Beberwyck, B. J.; Surendranath, Y.; Alivisatos, A. P. Cation Exchange: A Versatile Tool for Nanomaterials Synthesis. *J. Phys. Chem. C* **2013**, *117*, 19759−19770.
(39) Rivest, J. B.; Jain, P. K. Cation Exchange on the Nanoscale: An Emerging Technique for New Material Synthesis, Device Fabrication, and Chemical Sensing. *Chem. Soc. Rev.* **2013**, *42*, 89−96.
(40) Zanin, I. E.; Aleinikova, K. B.; Afanasiev, M. M.; Antipin, M. Y. Structure of Zn_3P_2. *J. Struct. Chem.* **2004**, *45*, 844−848.
(41) Misiewicz, J.; Szatkowski, J.; Mirowska, N.; Gumienny, Z.; Placzek-Popko, E. Zn_3P_2: New Material for Optoelectronic Devices. In *Proceedings SPIE 1561, Inorganic Crystals for Optics, Electro-Optics, and Frequency Conversion*; Bordui, P. F., Ed.; International Society for Optics and Photonics, 1991; pp 6−18.

DOI: 10.1021/acsnano.6b01266
ACS Nano 2016, 10, 4754−4762

(42) Misiewicz, J.; Wrobel, J. M.; Clayman, B. P. Lattice Modes of Zn_3P_2. *Solid State Commun.* **1988**, *66*, 747−750.
(43) Klimov, V. I. Quantization of Multiparticle Auger Rates in Semiconductor Quantum Dots. *Science (Washington, DC, U. S.)* **2000**, *287*, 1011−1013.
(44) Anderson, N. C.; Hendricks, M. P.; Choi, J. J.; Owen, J. S. Ligand Exchange and the Stoichiometry of Metal Chalcogenide Nanocrystals: Spectroscopic Observation of Facile Metal-Carboxylate Displacement and Binding. *J. Am. Chem. Soc.* **2013**, *135*, 18536−18548.
(45) Kats, A. *Indium Phosphide and Related Materials : Processing, Technology, and Devices*; Artech House: Boston, 1992.
(46) Owen, J. Nanocrystal Structure. The Coordination Chemistry of Nanocrystal Surfaces. *Science* **2015**, *347*, 615−616.
(47) Denton, A.; Ashcroft, N. Vegard's Law. *Phys. Rev. A: At., Mol., Opt. Phys.* **1991**, *43*, 3161−3164.
(48) Shin, H.; Jang, D.; Jang, Y.; Cho, M.; Park, K. High Resolution Imaging Analysis of CdSe/ZnS Core−shell Quantum Dots (QDs) Using Cs-Corrected HR-TEM/STEM. *J. Mater. Sci.: Mater. Electron.* **2013**, *24*, 3744−3748.
(49) Hossain, M. Z.; Medhekar, N. V.; Shenoy, V. B.; Johnson, H. T. Enhanced Quantum Confinement due to Nonuniform Composition in Alloy Quantum Dots. *Nanotechnology* **2010**, *21*, 095401.
(50) Alivisatos, A. P. Perspectives on the Physical Chemistry of Semiconductor Nanocrystals. *J. Phys. Chem.* **1996**, *100*, 13226−13239.
(51) Roduner, E. Size Matters: Why Nanomaterials Are Different. *Chem. Soc. Rev.* **2006**, *35*, 583−592.
(52) Wei, H. H.-Y.; Evans, C. M.; Swartz, B. D.; Neukirch, A. J.; Young, J.; Prezhdo, O. V.; Krauss, T. D. Colloidal Semiconductor Quantum Dots with Tunable Surface Composition. *Nano Lett.* **2012**, *12*, 4465−4471.
(53) Stein, J. L.; Mader, E. A.; Cossairt, B. M. Luminescent InP Quantum Dots with Tunable Emission by Post-Synthetic Modification with Lewis Acids. *J. Phys. Chem. Lett.* **2016**, *7*, 1315−1320.
(54) Nelson, J. B.; Riley, D. P. An Experimental Investigation of Extrapolation Methods in the Derivation of Accurate Unit-Cell Dimensions of Crystals. *Proc. Phys. Soc.* **1945**, *57*, 160−177.
(55) Williams, B. L.; Major, J. D.; Bowen, L.; Keuning, W.; Creatore, M.; Durose, K. A Comparative Study of the Effects of Nontoxic Chloride Treatments on CdTe Solar Cell Microstructure and Stoichiometry. *Adv. Energy Mater.* **2015**, *5*, 1500554.
(56) Nag, A.; Kovalenko, M. V.; Lee, J.-S.; Liu, W.; Spokoyny, B.; Talapin, D. V. Metal-Free Inorganic Ligands for Colloidal Nanocrystals: S2-, HS-, Se2-, HSe-, Te2-, HTe-, TeS3(2-), OH-, and NH2- as Surface Ligands. *J. Am. Chem. Soc.* **2011**, *133*, 10612−10620.
(57) Te Velde, G.; Bickelhaupt, F. M.; Baerends, E. J.; Fonseca Guerra, C.; van Gisbergen, S. J. A.; Snijders, J. G.; Ziegler, T. Chemistry with ADF. *J. Comput. Chem.* **2001**, *22*, 931−967.
(58) *ADF2014*, SCM, Theoretical Chemistry; Vrije Universiteit: Amsterdam, The Netherlands; http://www.scm.com.
(59) Wojdyr, M. *Debyer*, 2012; https://debyer.readthedocs.org/ (accessed Jan 2015).

DOI: 10.1021/acsnano.6b01266
ACS Nano 2016, 10, 4754−4762